Volume 1 | Number 1 | Jan 2013 | Pages 1–100

Journal of
Materials Chemistry C

Materials for optical and electronic devices
www.rsc.org/materialsC

ROYAL SOCIETY
OF CHEMISTRY

ROYAL SOCIETY
OF CHEMISTRY

www.rsc.org/materialsC

Journal of Materials Chemistry C

ARTICLE

Formation and local conduction of nanopits in BiFeO₃ epitaxial films†

Yajuan Zhao, Zhigang Yin,* Xingwang Zhang,* Zhen Fu and Jinliang Wu

The creation and manipulation of one-dimensional conducting channels, V-shaped nanopits, in the otherwise insulating BiFeO₃ epilayers are reported. The formation and thickness-dependent evolution of nanopits have a close correlation with the relaxation of shear strain that stems from the crystal symmetry mismatch between BiFeO₃ and the substrate. The local conduction at the nanopits exhibits a rectification behavior, and is governed by the interface-regulated Poole-Frenkel emission. The accumulation of oxygen vacancies near the nanopits not only modifies the interface barrier height, but also delivers donor states in the vicinity of the conduction band edge, and therefore leads to the locally enhanced nanopit conductance. Our findings provide a new insight into the interplay between defects and epitaxial strain, and open up a possible avenue for oxide nanoelectronics.

Introduction

Emergent behaviors in ferroic oxides that stem from defect engineering have attracted considerable interest in recent years.[1-3] The ferroic orders provide the capability to manipulate the functional properties by external fields, paving a new way for oxide nanoelectronics. For example, spontaneous polarization field in ferroelectrics can induce a migration of charged defects,[4] severely influencing the properties of the host materials. Charged defects were believed to contribute to the metallic or semiconducting conductance occurs at the two-dimensional (2D) topological boundaries, including domain walls and phase boundaries.[5-8] Based on these understandings, a number of experiments exemplified that the local conduction at such 2D boundaries can be electrically tuned,[9,10] making it highly desirable for designing new devices on the nanoscale. The formation, distribution and dynamics of defects in epilayers of ferroic oxides have a close correlation with the epitaxial strain.[11] For instance, it was revealed that oxygen vacancies (V_O), which result in a chemical expansion of the crystal lattice, offer a possible path to alleviate the tensile strain of oxide epitaxial films.[12] On the other hand, strain was demonstrated to have a crucial role in the formation and alignment of defects or defect dipoles,[11,13] and thereby strongly affects the physical behaviors of ferroic oxides.

However, some of the ferroic oxides do not follow the traditional understanding of thin-film strain. A paradigmatic example is BiFeO₃ (BFO), which can stay coherently on the SrTiO₃(001) substrates up to a thickness of ~100 nm.[14,15] According to classic elastic theory, the critical thickness beyond which strain relaxation starts is one order of magnitude smaller.[16] Similar phenomenon was also observed in the La₀.₃Sr₀.₇MnO₃ (LSMO) epitaxial films.[17] BFO and LSMO in their bulk forms have a rhombohedral structure,[18] and in addition to lattice mismatch, symmetry mismatch also occurs when they are deposited on cubic substrates. Recent works highlighted the role of symmetry mismatch in determining the growth mode, strain relaxation path, crystal structure and physical properties of epitaxial thin films.[19-21] Although significant progress has been made in the structural evolution of the symmetry-mismatched epitaxial systems,[22,23] the fundamental understanding on the interplay between the crystal symmetry, epitaxial strain and defects is still limited. Moreover, the distribution of defects and its influence on the overall properties of ferroic oxides, when the crystal symmetry change is involved, are far from being achieved.

In this study, nanopits, a new type of extended defects, were created in BFO epitaxial films. Careful structural analyses reveal a close correlation between the formation and evolution of nanopits and the relaxation of shear strain that is associated with symmetry mismatch. More interestingly, enhanced conduction was clearly observed at the nanopit regions, and an interface-regulated, Poole-Frenkel conduction mechanism was proposed. Our findings enrich the understanding of the interplay among defects, strain and crystal symmetry, and deliver the possibility for designing new oxide nanoelectronic devices.

Experimental section

Sample fabrication. The epitaxial BFO films were deposited by radio frequency magnetron sputtering on (001)-oriented Nb:SrTiO₃ [Nb:STO(001)] substrates using BFO powder target at a substrate temperature of 650 °C. The target was prepared by compressing the grinded Bi₂O₃ and Fe₂O₃ powder mixture (with molar ratio of 1.05:1) into a 80-mm-diameter copper cup, and no high-temperature

Key Lab of Semiconductor Materials Science, Institute of Semiconductors, Chinese Academy of Sciences, Beijing, 100083, P. R. China. E-mail: yzhg@semi.ac.cn and xwzhang@semi.ac.cn; Fax: 86-10-82304588
†Electronic Supplementary Information (ESI) available. See DOI: 10.1039/x0xx00000x

Please do not adjust margins

ARTICLE

sintering was performed to suppress severe Bi evaporation. The Nb:STO(001) substrates with miscut angles of ~0.1° were etched by buffered HF solution for 30 s, and then annealed in flowing oxygen atmosphere at 1000 °C for 1 h. As a result, single-unit-cell stepped surfaces with TiO_2 termination were obtained. Prior to deposition, the sputtering chamber was evacuated to a base pressure of 5×10^{-5} Pa, and then filled with the work gas of Ar and O_2 to a total pressure of 0.5 Pa. The oxygen partial pressure was adjusted to be 0.15 Pa by tuning the flow rates of Ar and O_2. A pre-sputtering of 15 min was performed before each growth in order to avoid contamination and warrant a uniform stoichiometry of the films.

Characterizations. X-ray diffraction (XRD) 2θ-θ curves and reciprocal space maps (RSMs) were collected at beamline 1W1A of Beijing Synchrotron Radiation Facility (BSRF) with wavelength λ = 1.5488 Å. The results of RSMs were shown in the plots of intensity with respect to q in the reciprocal lattice unit (r.l.u.), where $q = \lambda/2d$. Atomic force microscopy (AFM), conductive atomic force microscopy (CAFM) and Kelvin probe force microscopy (KPFM) measurements were carried out by a commercial scanning probe system (NT-MDT solver P47). For CAFM scanning, a DC tip bias ranging from -10 to 10 V was applied, and the current through the tip was read out by an amplifier. A Tecnai F30 transmission electron microscope was used for the cross-sectional studies at an acceleration voltage of 300 kV.

Results and discussion

Fig. 1 displays the XRD results of the BFO epitaxial films grown on Nb:STO(001) substrates with various thicknesses. The 2θ-θ curves (Fig. 1a) show that the (001) peak of BFO only slightly shifts towards the higher-angle side with the thickness increases from 10 to

270 nm. Moreover, all the (001) peak positions are far lower than that of the stress-free rhombohedral BFO, indicating these films are in a highly compressed state. Reciprocal space maps (RSMs) reveal no splitting in the (103) peak (Fig. S1a, ESI†) for the 10-nm-thick film, indicative of a tetragonal (Fig. S1b, ESI†) rather than the commonly observed M_A symmetry.[15] This tetragonal structure is a strain-distorted version of the rhombohedral parent phase and is quite different with the highly elongated one (with c/a ratio exceeding 1.2) stabilized on large-misfit substrates like $LaAlO_3$.[24] The extracted lattice parameters are $a = b$ = 3.905 Å, and c = 4.089 Å, suggesting the film is coherently strained on the Nb:STO substrate (a = 3.905 Å). As the film further thickens, out-of-plane (OP) domain tilt occurs as evidenced by the notable splitting in both the (103) and (113) reflections (Fig. 1b).[22] When OP domain tilt appears, the (00l) planes of the BFO domains are no longer parallel with the substrate surface. The (002) contour mappings (see Fig. S2 in the ESI†) suggest that the BFO lattice is tilted along the [110] and [1-10] axes. All possible structural variants, labelled as r_1, r_2, r_3 and r_4, are schematically shown in Fig. 1c. Based on these results, the lattice parameters of BFO can be extracted and the results are shown in Fig. 1d.

It is clearly visible in Fig. 1d that the changes in the lattice parameters are trivial, i.e., most of the lattice mismatch strain still remains, even under a large thickness of 270 nm. However, we strengthen here that besides lattice mismatch, symmetry mismatch also plays a key role in determining the strain states of the BFO/Nb:STO(001) films. BFO in its bulk form is a rhombohedrally distorted perovskite with lattice parameters $a = b = c$ = 3.96 Å, and $\alpha = \beta = \gamma \approx 89.4°$, whereas the Nb:STO substrate has a cubic structure. Due to the constraint of Nb:STO(001) surface with square symmetry,
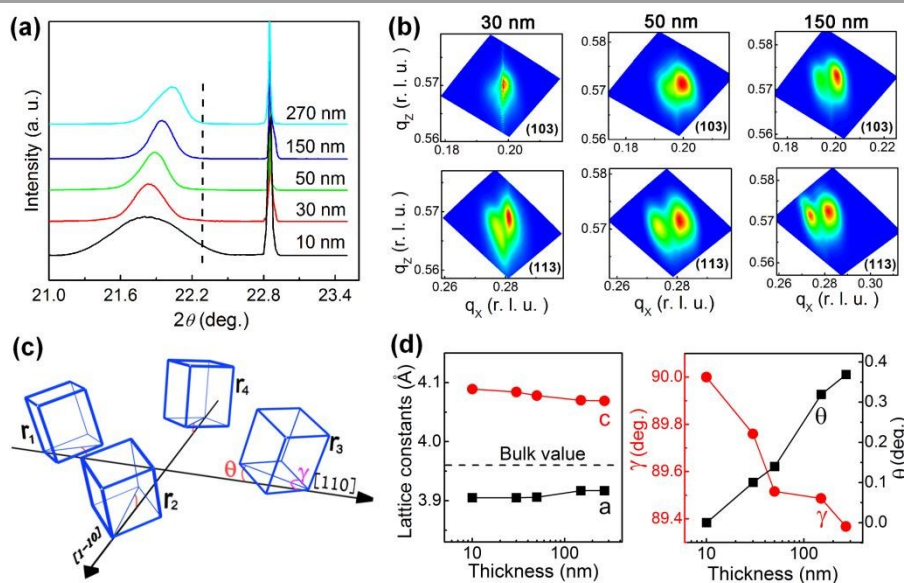

Fig. 1 (a) XRD 2ϑ-ϑ scans of the BFO/Nb:STO films with various thicknesses measured near the (001) reflection of Nb:STO; the dashed line indicates the (001) peak position of stress-free BFO. (b) RSMs collected around (103) and (113) reflections of BFO for the films with thickness of 30, 50 and 150 nm. (c) Schematic of the four possible domain variants derived from the RSMs, in which ϑ and γ denote the domain tilt angle and the in-plane rhombohedral angle, respectively. (d) Variations of the lattice parameters (left) and the ϑ and γ angles (right) as a function of film thickness.

Journal of Materials Chemistry C

ARTICLE

the coherent BFO layer has to take a tetragonal form at low thickness and thereafter, there emerges both normal and shear distortions for the rhombic lattice. The normal strain comes from lattice mismatch and the shear strain is associated with symmetry mismatch. The cooccurrence of normal and shear strains results in a very complex lattice relaxation process. Our results firmly show that the shear strain of BFO/Nb:STO(001) is preferentially released than the normal strain at the initial relaxation process. Domain tilt provides a feasible way to alleviate the constraint of the underlying substrate and, therefore, is effective in relieving the shear strain energy. Once domain tilt appears, the tetragonal symmetry of BFO is broken and the in-plane rhombohedral angle, γ, gradually decreases with the increase of the lattice tilt angle, θ, until the bulk value of γ is reached (Fig. 1d). The γ angle can be viewed as a measure of the lattice constraint of the substrate on BFO, and the lower the γ angle, the weaker the constraint of the substrate.

Fig. 2 shows the surface morphologies of the BFO/Nb:STO(001) films measured by AFM. The 10-nm-thick BFO film exhibits a layer-by-layer growth and inherits the atomically smooth, terrace-step topologies of the underlying Nb:STO(001) substrate (Fig. S3, ESI†). The root-mean-square (rms) roughness is merely 0.15 nm over a scan area of 2×2 μm^2, comparable with that of the substrate. As the film thickness goes up to 30 nm, randomly distributed nanopits were observed on the film surface without any pre-patterning or impurity seeding. Although the nanopits are more likely formed along the step edges due to the influence of Ehrlich-Schwoebel barrier,[25] the terrace-step structure is not necessarily

involved in the nanopit formation, typically when the terrace width is large enough.[26] Upon further increasing the film thickness to 150 nm, the nanopits significantly expand in size whereas the lateral density is drastically reduced. With additional deposition, some of the nanopits eventually meet with each other and deep trenches appear on the film surface. The evolution of nanopits is accompanied by a notable surface coarsening − the rms roughness sharply increases from 0.15 nm to 19 nm, as the film thickness rises from 10 to 270 nm. Tersoff and Legoues have elegantly demonstrated that the appearance of islands and nanopits offers two possible avenues to release the strain of epitaxial layers, and the latter is more effective at large lattice misfit.[27] Apparently, the formation and evolution of nanopits observed here are mainly associated with the shear strain rather than with the normal strain. We note that for the LSMO epilayers deposited on STO(001), nanopits were also found by Konstantinovic *et al.* without observable normal strain relaxation.[28] By contrast, triangle-shaped islands appear on the surface of BFO epilayer deposited on symmetry-matched STO(111) substrate (Fig. S4, ESI†). All these facts suggest that in addition to normal strain, shear strain provides another degree of freedom to tune the growth and the surface morphologies of epilayers.

It was reported that the nanopits provide possible dislocation nucleation sites and therefore, allow the elastic deformation of the epitaxial films.[27] Experimental works[29,30] revealed that, for group III-nitride epilayers, nanopits are indeed associated with the formation of dislocations. However, unlike III-nitrides, the unique relaxation path of BFO/Nb:STO(001) infers that dislocations are not
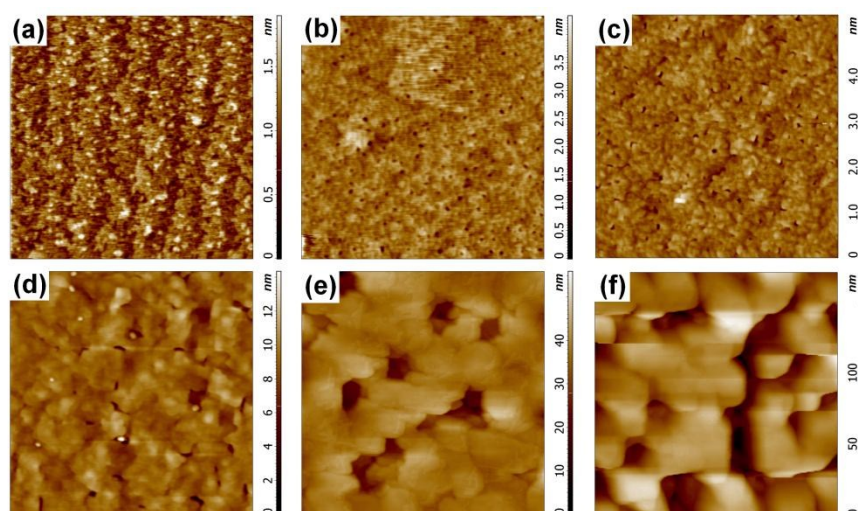

Fig. 2 AFM morphologies of BFO/Nb:STO films with thickness of 10 nm (a), 30 nm (b), 50 nm (c), 100 nm (d), 150 nm (e), and 270 nm (f). Upon raising the film thickness, the nanopit size is enlarged whereas the lateral density is significantly decreased. The scan area is 2×2 μm^2 for all the images.

Journal of Materials Chemistry C
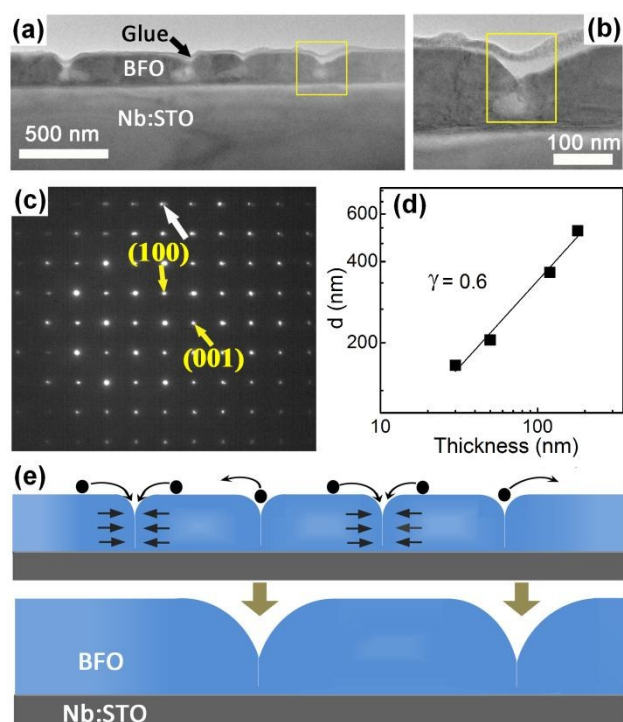
ARTICLE

Fig. 3 (a) Cross-sectional TEM image of the 150-nm-thick BFO/STO film, in which V-shaped nanopits were clearly resolved. (b) A magnified view of a typical nanopit shown in the selected area (yellow square) in (a). (c) SAED pattern obtained from the rectangular area in (b), in which the white arrow indicates the splitting of the high order reflection spots of BFO. (d) The least square fit of the average pit-to-pit spacing with respect to the film thickness. (e) Schematic of the thickness-dependent revolution of the nanopits; as the film growth proceeds, domain boundary propagation and domain coalescence appear which result in the nanopit enlargement and the reduction of nanopit density.

necessarily involved in the nanopit formation. Figure 3a shows a typical cross-sectional transmission electron microscopy (TEM) image of the 150-nm-thick sample, in which nanopits were clearly observed. The nanopits exhibit a V-shape and extend deeply into the epilayer, as resolved in a magnified view in Figure 3b. The selected-area electron diffraction (SAED, Fig. 3c) pattern along the zone axis of $[010]_{BFO}$ collected from a typical nanopit region (denoted by yellow square) in Fig. 3b shows a noticeable splitting for the high order reflection spots. In general, the spot splitting in the SAED pattern of BFO is associated with the lattice misorientation of adjacent domains (see Fig. 1c).[31] These facts imply that the nanopits are formed along the domain boundaries rather than within the

domains. Moreover, a least square fit of the average nanopit-to-nanopit spacing d (derived from Fig. 2) as a function of film thickness t gives rise to $d \propto t^{\gamma}$, with $\gamma \approx 0.6$ (Fig. 3d). In prior studies, the statistics of the domain size with respect to the film thickness yield a power law with similar scaling exponent,[32] again confirming that the nanopits observed in BFO are associated with domain boundaries.

The appearance of nanopits offers a way to relieve the strain energy at the cost of increasing the surface energy. As compared with the nanopits within the domains, the nanopits locate at the domain boundaries are beneficial for reducing the domain boundary energy,[33] and therefore are more energetically favorable. Moreover, we strengthen that there appear significant lattice distortion or even broken bonds at the boundaries between tilted domains of BFO, and thus the formation of nanopits at such boundaries can further compensate part of the surface energy increase. Consequently, nanopits tend to nucleate and growth at the domain boundaries for BFO deposited on the symmetry-mismatched substrates. As the growth proceeds, domain coalescence which follows the scaling law mentioned above occurs, giving rise to an increase of the domain size. As a result, some of the nanopits eventually vanish and thus the nanopit density is greatly reduced, during the domain boundary propagation (see Fig. 3e). These facts indicate that the adatoms can
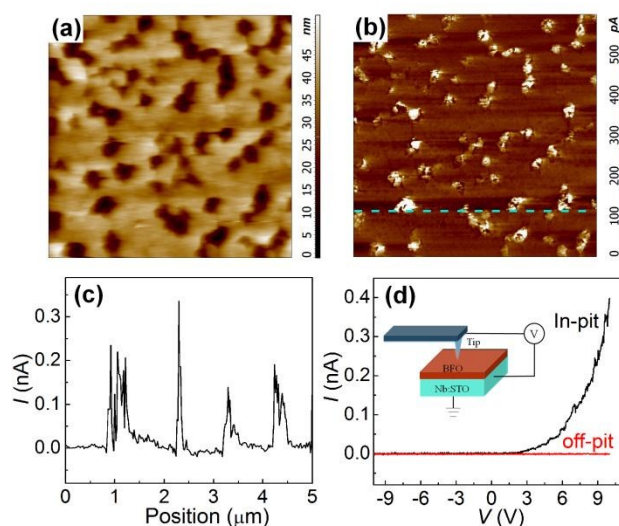

Fig. 4 (a) Morphologies and (b) CAFM images taken at the same area with a forward bias of +10 V. (c) Current line profile obtained along the dashed line in (b). (d) Typical I-V curves measured in and off the nanopit regions; inset is the schematic illustration of CAFM, where a bias is applied on the conducting tip. The scan area is 5×5 μm^2.

diffuse into (out of) the nanopits, depending on whether the nanopits locate off (in) the domain boundaries.

Most interestingly, the nanopits exhibit significantly enhanced electrical conduction, and a clear contrast to the matrix of BFO was observed, as revealed by the CAFM measurements on the 150-nm-thick BFO film (Fig. 4a and b). Off the nanopits the conductance is below 10 picoamperes when applying a bias of +10 V, suggesting an insulating nature of these regions. By sharp contrast, the conductance within the nanopits increases to several hundreds of picoamperes under the same bias. The current line profile shown in Fig. 4c again reveals that the current is markedly enhanced once the AFM tip moves into the nanopits. Local current versus voltage (*I-V*) curves (Fig. 4d) further confirm that only the nanopits can serve as conducting channels, and no remarkable current can be resolved in the BFO matrix. Moreover, The *I-V* curves of the nanopits exhibit a diode-like behavior, i.e., notable conduction can only be observed at forward bias, and when reverse bias is applied the nanopits stay in the insulating state.

To explore the origin of the BFO-nanopit conduction, temperature-dependent *I-V* curves were collected and the results are shown in Fig. 5a. We have analyzed these data with different mechanisms, including Fowler-Nordheim (FN) tunneling, Simmons-Richardson-Schottky (SRS) emission, Poole-Frenkel (PF) hopping, and space-charge-limited (SCL) conduction.[34] In the FN tunneling frame,[35] $\ln(I/V^2)$ has a linear dependence against $1/V$, where V and I stand for the applied voltage and the measured current, respectively. However, the strong temperature-dependence observed in Fig. 5a and Fig. S5a (ESI†) excludes the FN tunneling, since it is completely insensitive to temperature in nature.[34] On the other hand, the SCL conduction generally follows the relationship $I \propto V^n$, where the exponent $n \geq 2$. The absence of linearity in (n-1) versus T^{-1} (the inset of Fig. S5b, ESI†) in the case of $n > 2$, where T is the measured temperature, indicates the SCL conduction is not the underlying mechanism for the nanopit conduction.[34]
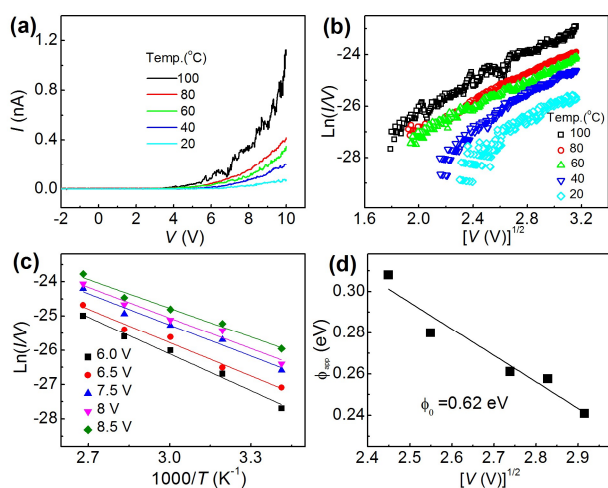
SRS and PF emissions have similar mathematical expressions, i.e., $\ln(I/V) \propto V^{1/2}$, although their physical origins are quite different.[34] The $\ln(I/V) \propto V^{1/2}$ plots of the data presented in Fig. 5b show a reasonably good linearity, indicating that SRS or PF emission may be the possible answer. The value of the optical dielectric constant, which can be extracted by the $\ln(I/V) \propto V^{1/2}$ fitting, is commonly used to determine whether SRS or PF emissions are relevant.[7] However, this method applies to the metal/semiconductor plate-like junction, but not hold for the irregular nanopits with inhomogeneous current distribution studied here. To gain more insight into the nature of the nanopit conduction, we turn to a detailed analysis of the barrier height under the SRS and PF schemes. Using the method in Ref. 36, a Schottky barrier height of 0.58 eV for the Pt/BFO junction was derived (Fig. S6, ESI†). By comparison, a much larger barrier for the Pt/BFO junction is anticipated (Fig. S7a, ESI†), on basis of the reported electron affinity and band gap values of BFO[5] as well as the work function of Pt-coated tip.[37] The rather low barrier height obtained here is associated with a downward band bending at the BFO-nanopit surface and therefore, the lack of an electron blocking layer in BFO. Under this condition, the electrical conduction at forward bias is bulk-limited, making the interface-limited SRS mechanism quite unlikely. To test whether the PF hopping is relevant, the dependence of $\ln(I/V)$ on $1/T$ was plotted and the results are shown in Fig. 5c. By linearly fitting these data we can obtain Φ_{app} (Fig. 5d), denoted by the slope of the lines. In the mathematical expression of PF emission, $\exp(T^{-1} \cdot \Phi_{app})$ is the exponent term. An extrapolation of the linear relationship between Φ_{app} and $V^{1/2}$ to $V^{1/2} = 0$ yields a PF barrier height of 0.62 eV. We note that Clark *et al.*[38] have theoretically predicted the presence of shallow states, 0.6 eV below the bottom of the conduction band, by introducing V_O into BFO. Moreover, an ionization energy of 0.68 eV for V_O was observed by Yang *et al.* in BFO thin epitaxial films.[39] These values are all in good agreements with the PF barrier height obtained here.

Here we note that the PF emission is a bulk-limited mechanism, and it alone cannot account for the rectifying character observed in Fig. 4. Obviously, the rectification is associated with the interface-limited processes. Although a large Schottky barrier is expected (Fig. S7a, ESI†), we note that it can be greatly reduced by the n-type doping of the BFO nanopit surface. It was reported previously that due to the accumulation of V_O, the barrier height at the BFO domain walls can be lowered by more than 1 eV.[7] Taking into account the presence of sufficient amount of V_O at the nanopit surface, a schematic of the band structure at the Pt/BFO-nanopit junction is obtained (see Fig. S7b in the ESI†, for details). As reverse bias is applied, the leakage current is fairly small since very few electrons in Pt have enough energy to surmount the barrier. Under forward bias, the barrier for the electrons travelling from BFO to the Pt tip is negligible, even when the forward bias approaches 0 V. That is, the current is determined by the series resistance rather than by the barrier at the Pt/BFO interface when forward bias is applied. Therefore, the notable conduction observed at forward bias is not interface-limited but bulk-limited, and our results show that it is dominated by the PF mechanism.

All these discussions point to an interface-regulated PF conduction, i.e., the interface barrier results in the rectification behavior, while the conduction within the nanopits is governed by

Fig. 5 (a) Temperature-dependent *I-V* curves collected at a BFO nanopit. (b) ln (*I/V*) versus V plots of the data shown in (a). (c) The dependence of ln(*I/V*) on 1/*T* for various voltages; the values of Φ_{app} can be obtained by linearly fitting these data. (d) The Φ_{app} versus $V^{1/2}$ plots; an extrapolation of the linear relationship between Φ_{app} and $V^{1/2}$ to $V^{1/2} = 0$ yields a barrier height of 0.62 eV.
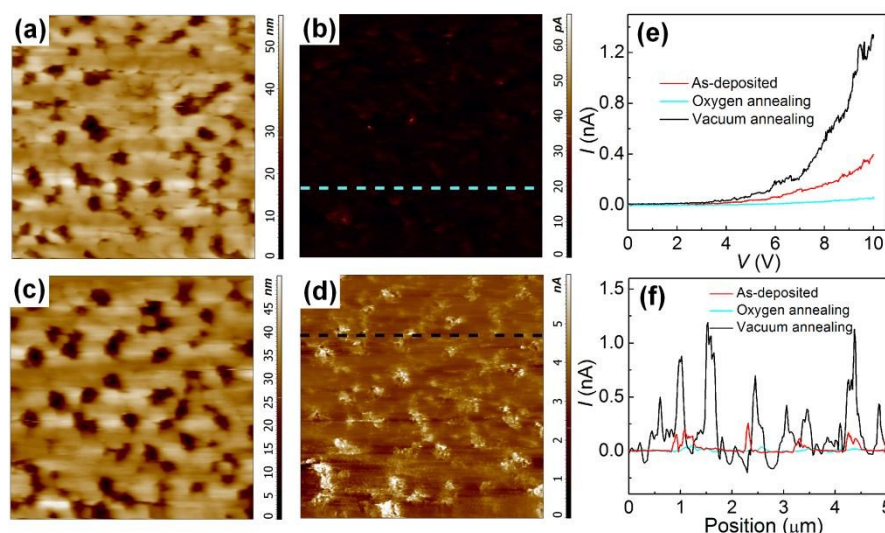
Journal of Materials Chemistry C

ARTICLE

Fig. 6 Morphologies [(a) and (c)] and CAFM images [(b) and (d)] of the 150-nm-thick BFO films annealed in flowing oxygen (upper) and in vacuum (lower). *I-V* curves measured at the nanopit regions (e) and current line profiles (f) for the as-grown [dashed line in Fig. 4(b)], oxygen-annealed [dashed line in (b)] and vacuum-annealed [dashed line in (d)] samples. The scan area is 5×5 μm^2.

the PF emission. This scenario highlights the key role of V_O – it not only modifies the interface barrier height, but also provides the electron reservoir for conduction. Oxygen vacancies supply donor states near the Fermi level, and the ionization of V_O generates electrons in the conduction band of BFO. Owing to the downward band bending of BFO induced by V_O,[40] the generated electrons are accumulated and constraint near the nanopit surface, leading to the occurrence of surface metallization[41,42] of the BFO nanopits. Although the interface barrier height is greatly reduced by V_O, it can still impede the electrons in the Pt tip locate near the interface from entering into BFO under reverse bias, giving rise to the rectification behavior shown in Fig. 4.

In order to get more evidence, annealing treatments were performed at 500 °C under vacuum and in the flowing oxygen atmosphere, and their influences on the nanopit conduction were studied (Fig. 6a-d). No detectable nanopit conduction was observed for the oxygen annealed sample, and the conduction level within the nanopits is similar with that off the pits. By sharp contrast, a considerably enhanced conduction was observed at the nanopits for the film annealed in vacuum. Compared with the as-grown film, the measured nanopit current signal is increased by one order of magnitude, reaching to the nanoampere level. These observations are also corroborated by the *I-V* curves (Fig. 6e) and the current line profiles (Fig. 6f) for the as-grown, oxygen-annealed and vacuum-annealed samples. Moreover, the transition between the high- and low-level conduction is reversible, when sequential anneals in vacuum and flowing oxygen atmosphere were performed (Fig. S8,

ESI†). All these results support that V_O has a key role in the observed nanopit conductance.

It is known that the appearance of V_O can induce a decrease of the work function[43] and as a result, an increase of the surface potential. KPFM measurements (Fig. S9, ESI†) indeed reveal a rather inhomogeneous surface potential distribution. Moreover, it was found that the surface potential values are much higher in the nanopits than in other regions. Such observations corroborate that the concentration of V_O is higher in the nanopits than in other surface regions of the film, i.e., V_O is more inclined to accumulate at the nanopits. These results explain why the notable conduction is restricted to the nanopit regions, while the top surface of the films including other domain boundary areas still remains insulating. The attachment of V_O at the nanopits suggests a reduced formation energy of V_O near the nanopits regions, possibly due to the influence of the coordination environment. Recent theoretical works[44,45] have revealed that, for transition metal oxides, the formation energy of V_O is strongly dependent on the coordination number. To achieve a fully understanding on this issue, first principles calculations are required to explore the formation energies of V_O on various crystallographic surfaces of BFO.

The creation and device applications of local conduction channels in the otherwise insulating ferroelectrics have received considerable interest in recent years.[1-10] However, most of the experimental and theoretical studies so far are restricted to 2D objects such as domain walls. The funding of enhanced conductance at nanopits of BFO provides a new, 1D conduction entity, which is of vital importance

for the implementations in electronic devices.[3] Also worth note is that the formation and evolution of nanopits are intrinsically linked with the strain relaxation process, providing additional degree of freedom to tune the distribution and function of the conduction channels. Moreover, we strengthen that although BFO has excellent physical properties including high spontaneous polarization, its usage is severely limited by the occurrence of considerable leakage current that is originated from V_O.[13] Our results show that V_O has a tendency to attach on the nanopit surface and can be easily annihilated by oxygen annealing treatments. This funding offers a feasible way to synthesize nearly V_O-free BFO films, and therefore is technologically important for future ferroelectric applications.

Conclusions

In summary, we have reported the formation of nanopits on the surfaces of BFO epitaxial films deposited on Nb:STO(001) substrates. These nanopits locate at the domain boundaries, and with increasing the film thickness the nanopit size is considerably enlarged whereas the lateral density is drastically reduced. We reveal that shear strain, which is originated from the crystal symmetry mismatch between the epilayer and the substrate, strongly influences the formation and evolution of the nanopits. Considerably enhanced local conductance with a diode-like behavior was clearly resolved at the nanopit regions by CAFM and the underlying mechanism was explored based on the measurements at elevated temperatures. Our results show that the accumulation of V_O can reduce the interface barrier height and provide donor states near the bottom of the conduction band, and therefore lead to the interface-dependent PF conduction. The annealing treatments under oxygen-rich and -poor environments and the surface potential characterizations confirm the key role of V_O on the nanopit local conductance.

Acknowledgements

Notes and references

1 J. Seidel, L. W. Martin, Q. He, Q. Zhan, Y. H. Chu, A. Rother, M. E. Hawkridge, P. Maksymovych, P. Yu, M. Gajek, N. Balke, S. V. Kalinin, S. Gemming, F. Wang, G. Catalan, J. F. Scott, N. A. Spaldin, J. Orenstein, R. Ramesh, *Nat. Mater.* 2009, **8**, 229-234.

2 Q. He, C. H. Yeh, J. C. Yang, G. Singh-Bhalla, C. W. Liang, P. W. Chiu, G. Catalan, L. W. Martin, Y. H. Chu, J. F. Scott, R. Ramesh, *Phys. Rev. Lett.* 2012, **108**, 067203.

3 N. Balke, B. Winchester, W. Ren, Y. H. Chu, A. N. Morozovska, E. A. Eliseev, M. Huijben, R. K. Vasudevan, P. Maksymovych, J. Britson, S. Jesse, I. Kornev, R. Ramesh, L. Bellaiche, L. Q. Chen, S. V. Kalinin, *Nat. Phys.* 2012, **8**, 81-88.

4 Y. M. Kim, A. Morozovska, E. Eliseev, M. P. Oxley, R. Mishra, S. M. Selbach, T. Grande, S. T. Pantelides, S. V. Kalinin, A. Y. Borisevich, *Nat. Mater.* 2014, **13**, 1019-1025.

5 J. Seidel, P. Maksymovych, Y. Batra, A. Katan, S. Y. Yang, Q. He, A. P. Baddorf, S. V. Kalinin, C. H. Yang, J. C. Yang, Y. H. Chu, E. K. H. Salje, H. Wormeester, M. Salmeron, R. Ramesh, *Phys. Rev. Lett.* 2010, **105**, 197603.

6 W. D. Wu, Y. Horibe, N. Lee, S. W. Cheong, J. R. Guest, *Phys. Rev. Lett.* 2012, **108**, 077203.

7 S. Farokhipoor, B. Noheda, *Phys. Rev. Lett.* 2011, **107**,127601.

8 J. Seidel, M. Trassin, Y. Zhang, P. Maksymovych, T. Uhlig, P. Milde, D. Kohler, A. P. Baddorf, S. V. Kalinin, L. M. Eng, X. Q. Pan, R. Ramesh, *Adv. Mater.* 2014, **26**, 4376-4380.

9 P. Maksymovych, A. N. Morozovska, P. Yu, E. A. Eliseev, Y. H. Chu, R. Ramesh, A. P. Baddorf, S. V. Kalinin, *Nano Lett.* 2012, **12**, 209-213.

10 Y. H. Hsieh, E. Strelcov, J. M. Liou, C. Y. Shen, Y. C. Chen, S. V. Kalinin, Y. H. Chu, *ACS Nano* 2013, **7**, 8627-8633.

11 A. P. Damodaran, W. Breckenfeld, Z. H. Chen, S. Lee, L. W. Martin, *Adv. Mater.* 2014, **26**, 6341-6347.

12 U. Aschauer, R. Pfenninger, S. M. Selbach, T. Grande, N. A. Spaldin, *Phys. Rev. B* 2013, **88**, 054111.

13 D. Lee, B. C. Jeon, A. Yoon, Y. J. Shin, M. H. Lee, T. K. Song, S. D. Bu, M. Kim, J. S. Chung, J. G. Yoon, T. W. Noh, *Adv. Mater.* 2014, **26**, 5005-5011.

14 D. H. Kim, H. N. Lee, M. D. Biegalski, H. M. Christen, *Appl. Phys. Lett.* 2008, **92**, 012911.

15 C. J. M. Daumont, S. Farokhipoor, A. Ferri, J. C. Wojdel, J. Iniguez, B. J. Kooi, B. Nohedra, *Phys. Rev. B* 2010, **81**, 144115.

16 R. People, J. C. Bean, *Appl. Phys. Lett.* 1985, **47**, 322-324.

17 Z. Konstantinovic, J. Santiso, D. Colson, A. Forget, L. Balcells, B. Martinez, *J. Appl. Phys.* 2009, **105**, 063919.

18 Z. Fu, Z. G. Yin, N. F. Chen, X. W. Zhang, Y. J. Zhao, Y. M. Bai, Y. Chen, H. H. Wang, X. L. Zhang, J. L. Wu, *Appl. Phys. Lett.* 2014, **104**, 052908.

19 X. D. Qi, M. Wei, Y. Li, Q. X. Jia, D. Zhi, J. Gho, M. G. Blamire, J. L. MacManus-Driscoll, *Appl. Phys. Lett.* 2005, **89**, 071913.

20 D. L. Proffit, H. W. Jang, S. Lee, C. T. Nelson, X. Q. Pan, M. S. Rzchowski, C. B. Eom, *Appl. Phys. Lett.* 2008, **93**, 111912.

21 Z. Fan, J. Wang, M. B. Sullivan, A. Huang, D. J. Singh, K. P. Ong, *Sci. Rep.* 2014, **4**, 4631.

22 H. J. Liu, P. Yang, K. Yao, J. Wang, *Appl. Phys. Lett.* 2010, **96**, 012901.

23 U. Gebhardt, N. V. Kasper, A. Vigliante, P. Wochner, H. Dosch, F. S. Razavi, H. U. Habermeier, *Phys. Rev. Lett.* 2007, **98**, 096101.

24 R. J. Zeches, M. D. Rossell, J. X. Zhang, A. J. Hatt, Q. He, C.-H. Yang, A. Kumar, C. H. Wang, A. Melville, C. Adamo, G. Sheng, Y.-H. Chu, J. F. Ihlefeld, R. Erni, C. Ederer, V. Gopalan, L. Q. Chen, D. G. Schlom, N. A. Spaldin, L. W. Martin, R. Ramesh, *Science* 2009, **326**, 977-980.

25 M. G. Legally, Z. Y. Zhang, *Nature* 2002, **417**, 907-910.

26 Z. Konstantinovic, J. Santiso, L. Balcells, B. Martinez, *Nanotechnology* 2010, **21**, 465601.

27 J. Tersoff, F. K. LeGoues, *Phys. Rev. Lett.* 1994, **72**, 3570-3573.

28 Z. Konstantinovic, J. Santiso, L. Balcells, B. Martiinez, *Small* 2009, **5**, 265-271.

29 Z. L. Weber, Y. Chen, S. Ruvimov, J. Washburn, *Phys. Rev. Lett.* 1997, **79**, 2835-2838.

30 F. Liu, R. Collazo, S. Mita, Z. Sitar, G. Duscher, *Adv. Mater.* 2008, **20**, 134-137.

31 Z. H. Chen, Y. J. Qi, L. You, P. Yang, C. W. Huang, J. L. Wang, T. Sritharan, L. Chen, *Phys. Rev. B* 2013, **88**, 054114.

32 G. Cantalan, H. Bea, S. Fusil, M. Bibes, P. Paruch, A. Barthelemy, J. F. Scott, *Phys. Rev. Lett.* 2008, **100**, 027602.

33 Y. Wang, C. Nelson, A. Melville, B. Winchester, S. Shang, Z. K. Liu, D. G. Schlom, X. Q. Pan, L. Q. Chen, *Phys. Rev. Lett.* 2013, **110**, 267601.

34 J. Guyonnet, I. Gaponenko, S. Gariglio, P. Paruch, *Adv. Mater.* 2011, **23**, 5377-5382.

35 B. H. Fowler, L. W. Nordheim, *Proc. Roy. Soc. A* 1928, **119**, 173-181.

36 L. Pintilie, I. Vrejoiu, D. Hesse, G. LeRhun, M. Alexe, *Phys. Rev. B* 2007, **75**, 104103.

37 N. Satoh, S. Katori, K. Kobayashi, S. Watanabe, T. Fujii, K. Matsushige, H. Yamada, *J. Appl. Phys.* 2011, **109**, 114306.

38 S. J. Clark, J. Robertson, *Appl. Phys. Lett.* 2009, **94**, 022902.

39 H. Yang, M. Jain, N. Suvorova, H. Zhou, H. M. Luo, D. M. Feldman, P. C. Dowden, P. F. DePaula, S. R. Foltyn, Q. X. Jia, *Appl. Phys. Lett.* 2007, **91**, 072911.

40 S. M. Walker, A. D. L. Torre, F. Y. Bruno, A. Tamai, T. K. Kim, M. Hoesch, M. Shi, M. S. Bahramy, P. D. C. King, F. Baumberger, *Phys. Rev. Lett.* 2014, **113**, 177601.

41 W. Meevasana, P. D. C. King, R. H. He, S. K. Mo, M. Hashimoto, A. Tamai, P. Songsiriritthigul, F. Baumberger, Z. X. Shen, *Nat. Mater.* 2011, **10**, 114-118.

42 A. F. Santander-Syro, O. Copie, T. Kondo, F. Fortuna, S. Pailhes, R. Weht, X. G. Qiu, F. Bertran, A. Nicolaou, A. Taleb-Ibrahimi, P. L. Fevre, G. Herranz, M. Bibes, N. Reyren, Y. Apertet, P. Lecoeur, A. Barthelemy, M. J. Rozenberg, *Nature* 2011, **469**, 189-194.

43 M. T. Greiner, L. Chai, M. G. Helander, W. M. Tang, Z. H. Lu, *Adv. Funct. Mater.* 2012, **22**, 4557-4568.

44 A. Walsh, *Appl. Phys. Lett.* 2011, **98**, 261910.

45 S. Lany, A. Zakutayev, T. O. Mason, J. F. Wagner, K. P. Poeppelmeier, J. D. Perkins, J. J. Berry, D. S. Ginley, A. Zunger, *Phys. Rev. Lett.* 2012, **108**, 016802.
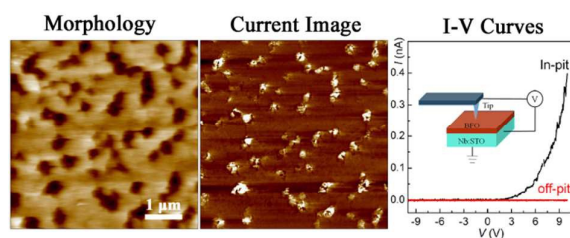
Table of Contents for

Formation and local conduction of nanopits in BiFeO₃ epitaxial films

Yajuan Zhao, Zhigang Yin,* Xingwang Zhang,* Zhen Fu, and Jinliang Wu

Key Lab of Semiconductor Materials Science, Institute of Semiconductors, Chinese Academy of Sciences, Beijing, 100083, P. R. China

*Corresponding author. E-mail: yzhg@semi.ac.cn and xwzhang@semi.ac.cn

Nanopits are formed in the BiFeO₃ epilayers and enhanced conductance, governed by the interface-regulated Poole-Frenkel emission, occurs at the nanopits.